

## Significantly enhanced oxygen reduction activity of Cu/CuN<sub>x</sub>C<sub>y</sub> co-decorated ketjenblack catalyst for Al-air batteries

Fuzhi Li, Jingsha Li, Qiuju Feng, Jun Yan, Yougen Tang and Haiyan Wang

Citation: *Journal of Energy Chemistry* **27**, 419 (2018); doi: 10.1016/j.jechem.2017.12.002

View online: <http://engine.scichina.com/doi/10.1016/j.jechem.2017.12.002>

View Table of Contents: <http://engine.scichina.com/publisher/scp/journal/JEC/27/2>

Published by the [Science China Press](#)

---

### Articles you may be interested in

[Synthesis and electrochemical properties of dual doped spinels LiNi<sub>x</sub>Al<sub>y</sub>Mn<sub>2-x-y</sub>O<sub>4</sub> via facile novel chelated sol-gel method as possible cathode material for lithium rechargeable batteries](#)

Journal of Energy Chemistry **26**, 101 (2017);

[Synthesis and evaluation as CO<sub>2</sub> chemisorbent of the Li<sub>5</sub>\(Al<sub>1-x</sub>Fe<sub>x</sub>\)O<sub>4</sub> solid solution materials: Effect of oxygen addition](#)

Journal of Energy Chemistry **26**, 948 (2017);

[Enhanced CO catalytic oxidation by Sr reconstruction on the surface of La<sub>x</sub>Sr<sub>1-x</sub>CoO<sub>3-δ</sub>](#)

Science Bulletin **62**, 658 (2017);

[Pore structure of new composite adsorbent SiO<sub>2</sub>·xH<sub>2</sub>O·yCaCl<sub>2</sub> with high uptake of water from air](#)

Science in China Series E-Technological Sciences **46**, 551 (2003);

[Spray pyrolysis synthesis of nickel-rich layered cathodes LiNi<sub>1-2x</sub>Co<sub>x</sub>Mn<sub>x</sub>O<sub>2</sub> \(x = 0.075, 0.05, 0.025\) for lithium-ion batteries](#)

Journal of Energy Chemistry **27**, 447 (2018);

---



# Significantly enhanced oxygen reduction activity of Cu/CuN<sub>x</sub>C<sub>y</sub> co-decorated ketjenblack catalyst for Al-air batteries

Fuzhi Li<sup>a,b</sup>, Jingsha Li<sup>a</sup>, Qiuju Feng<sup>c</sup>, Jun Yan<sup>a</sup>, Yougen Tang<sup>a,d,\*</sup>, Haiyan Wang<sup>a,d,\*</sup>

<sup>a</sup> College of Chemistry and Chemical Engineering, Central South University, Changsha 410083, Hunan, China

<sup>b</sup> College of Life Sciences and Chemistry, Hunan University of Technology, Zhuzhou 412008, Hunan, China

<sup>c</sup> College of Chemistry and Chemical Engineering, Jishou University, Jishou 416000, Hunan, China

<sup>d</sup> Hunan Provincial Key Laboratory of Efficient and Clean Utilization of Manganese Resources, Central South University, Changsha 410083, Hunan, China

## ARTICLE INFO

### Article history:

Received 29 October 2017

Revised 1 December 2017

Accepted 3 December 2017

Available online 19 December 2017

### Keywords:

Al-air batteries

Oxygen reduction reaction

Electrocatalyst

Copper nanoparticles

Copper–nitrogen doping

## ABSTRACT

Highly efficient and non-precious catalysts are imperative for oxygen reduction reaction (ORR) to replace Pt/C. Anchoring efficient active species to carbon supports is a promising and scalable strategy. Here we synthesize Cu nanoparticles and noncrystalline CuN<sub>x</sub>C<sub>y</sub> species co-decorated ketjenblack (KB) carbon catalyst (denoted as Cu-N-KB-acid) by a facile and scalable method using copper sulfate, melamine, and KB as raw materials. An initial one-pot hydrothermal treatment is designed before pyrolysis process to achieve the good distribution of Cu and melamine on KB via a possible chelation effect. Owing to the synergistic effect of Cu and CuN<sub>x</sub>C<sub>y</sub> on KB, this composite catalyst displays excellent ORR catalytic activity in alkaline solution, which is comparable to the commercial 20% Pt/C. When used as a catalyst in a home-made Al-air battery, it shows a stable discharge voltage of 1.47 V at a discharge density of 50 mA cm<sup>-2</sup>, a little higher than that of Pt/C (1.45 V).

© 2017 Science Press and Dalian Institute of Chemical Physics, Chinese Academy of Sciences. Published by Elsevier B.V. and Science Press. All rights reserved.

## 1. Introduction

Owing to the sluggish reaction kinetics, oxygen reduction reaction (ORR) is considered as the major bottleneck for developing advanced metal air batteries [1–6]. To address such issue, Pt-based catalysts are widely used as the state-of-the-art catalyst. However, their rare reserve, high price and sensitivity to CO poisoning have inspired lots of researches to pursue low cost and highly efficient candidate to replace the commercial Pt/C catalyst. Among these catalysts, carbon materials functionalized with nitrogen [7–9] or transition metals and nitrogen (marked as TM-N-C or TMNC, where TM = Fe, Co, Cu, etc., N = nitrogen, C = carbon) have been reported as two competitive classes of non-precious catalysts for the ORR [10–12]. Fe-N-C catalysts have attracted particular attention owing to their comparable ORR catalytic activity to commercial Pt/C [11,13–17]. Although the nature of the active sites in TM-N-C composite still remains controversial, it is well accepted that both the non-crystalline TMN<sub>x</sub>C<sub>y</sub> moieties and the crystalline metal-based nanoparticles (e.g. M, M<sub>3</sub>C, where M = metal) encased in the surrounding graphitic carbon layers are proposed as the main active sites [18].

Recently, the copper-based catalysts have attracted much attention because of their low overpotential for O<sub>2</sub> reduction to H<sub>2</sub>O [3,19], high electronic conductivity (just less than Ag), low price and relatively large abundance [8]. Cho et al. [20] developed nano-CuS@Cu-BTC (BTC = 1,3,5-benzenetricarboxylate) composite using Cu-BTC and thioacetamide as raw materials, which exhibited an onset potential of 0.91 V (vs. RHE, reversible hydrogen electrode) and quasi-four-electron transfer pathway (*n* = 3.82). Periasamy et al. [21] prepared Cu<sub>9</sub>S<sub>8</sub>/CNTs nanocomposites with an onset potential of –0.18 V (vs. SCE, saturated calomel electrode) and a near four-electron pathway in alkaline media for ORR. Wu et al. [19] prepared Cu-N@C catalyst utilizing copper phthalocyanine (CuPc) and dicyandiamide, and found that the highly exposed Cu(I)-N active sites greatly promoted the ORR catalytic activity. Cu, N-co-doped carbons (Cu-N-C) derived from Cu-containing ZIF-8 also exhibited good performance for ORR due to the Cu, N-doping and porous structure [8]. A highly efficient copper-containing catalyst was synthesized by embedding 5-nitrophthalocyanine into polyvinylimidazole (PVI), which wrapped around the carbon nanotubes [3]. Although these copper based catalysts showed good catalytic activity for ORR, the preparation process often involved expensive materials such as CuPc [19], ZIF-8 [8], CNT [21], BTC [20], 5-nitrophthalocyanine and PVI (polyvinylimidazole) [3]. Therefore, it is indispensable to improve the catalytic performance with cheap raw materials as much as possible. Nitrogen doping is an essential

\* Corresponding authors at: College of Chemistry and Chemical Engineering, Central South University, Changsha 410083, Hunan, China.

E-mail addresses: [ygtang@csu.edu.cn](mailto:ygtang@csu.edu.cn) (Y. Tang), [wanghy419@126.com](mailto:wanghy419@126.com) (H. Wang).

step in the preparation of TM-N-Cs for ORR. In general, nitrogen doping was gained by the pyrolysis of nitrogen-containing precursors, such as melamine [22–24], 1-octadecylamine [25], cyanamide, dicyandiamide and polyaniline [18,26–28]. These precursors generally generate a great deal of gases during pyrolysis. When these gases flow out, they take samples away and lead to a relatively low yield.

In this work, we introduced a facile and scalable way to synthesize Cu and  $\text{CuN}_x\text{C}_y$  co-decorated ketjenblack (KB) composite (denoted as Cu-N-KB-acid) using low cost materials such as copper sulfate, melamine and KB. Hydrothermal process was first employed before the pyrolyzation to achieve better distribution of the doped Cu and N. In the meantime, the pyrolyzation process was optimized by wrapping the porcelain boat with copper foil, resulting in much higher yield (~32.32% for wrapped and ~5.01% for unwrapped). Owing to the interaction of  $\text{CuN}_x\text{C}_y$ , Cu nanoparticles and KB supports, the as-prepared Cu-N-KB-acid exhibited significantly improved ORR activity in 0.1 M KOH solution, which is comparable to the commercial Pt/C (Johnson Matthey, 20 wt%). When used in home-made Al-air batteries, it also showed a little higher practical discharge voltage.

## 2. Experimental

### 2.1. Preparation of catalysts

All chemical reagents used in this work are of analytical grade and without further purification. First, 0.2 g of KB was added into a homogenous aqueous solution containing 1.0 g of copper sulfate, then magnetically stirred at least for 10 min. Second, 1.1 g of melamine was added into the mixed solution, then stirred for 30 min. Third, the resulting solution was enclosed into a 100 mL Teflon lined stainless steel shell autoclave, heated to 120 °C in an oven and kept at the temperature for 24 h. After it was cooled to room temperature naturally, the as obtained product was filtrated under vacuum with membrane of 0.15 μm pore diameter and dried overnight at 80 °C. After carefully ground by agate mortar for more than 5 min, the resulting powder was transferred to a piece of porcelain boat, which was then covered with another piece of porcelain boat and further wrapped by copper foil. The treated porcelain boat was placed into a tube furnace and then heated to 650 °C for 2 h at a heating rate of 5 °C min<sup>-1</sup> in argon flow. After that, it was naturally cooled to room temperature. Finally, the obtained sample was treated with 3 M HCl at 80 °C for 6 h with continuous agitation to remove unstable phases [1,12]. After filtration, washing and drying, the collected sample was heated again at 650 °C for 1 h to repair the catalyst surface and reinforce the grain phases [29,30]. The as prepared catalyst was denoted as Cu-N-KB-acid. For comparison, the sample without acid treatment was denoted as Cu-N-KB.

We also synthesized three control samples, N-KB, Cu-N and Cu-KB. For N-KB, all procedures were the same with Cu-N-KB but without the addition of copper sulfate. For Cu-N, all procedures were the same with Cu-N-KB but no KB was added. For Cu-KB, all procedures were the same with Cu-N-KB but no melamine was added. It should be noted that no acid treatment and no subsequent pyrolysis procedure were employed for these control samples.

### 2.2. Physical characterization of catalysts

X-ray diffractometer (Rigaku D/Max 2550) was used to characterize the structures of the as-prepared samples. The morphologies and microstructures of these catalysts were studied us-

ing transmission electron microscopy (TEM, Titan G2 60-300). X-ray photoelectron spectroscopy (XPS) test was detected on K-Alpha1063 spectrometer. Nitrogen adsorption/desorption isotherms were recorded using Quantachrome autosorb-1. The Raman spectrum was tested by Raman Spectrophotometer (Labram-010,  $\lambda_{\text{ex}} = 632 \text{ nm}$ ).

### 2.3. Electrochemical measurements

For electrochemical measurements, 6 mg of as-prepared catalyst was dispersed in 950 μL anhydrous ethanol by sonication for 20 min, then 50 μL of nafion solution (5 wt%) was added and sonicated for another 20 min to get a homogeneous catalytic ink. 10 μL of the ink was loaded onto the surface of glassy carbon disk, and the catalyst loading is 0.2437 mg cm<sup>-2</sup>. For comparison, the commercial 20 wt% Pt/C (Johnson Matthey) was also prepared with the same method.

Linear sweep voltammetry (LSV) and cyclic voltammetry (CV) were performed using a double fluid boundary Ag/AgCl electrode as the reference electrode, and a platinum wire as the counter electrode in 0.1 M KOH solution saturated with oxygen on a CHI760E electrochemical workstation. All potentials were finally converted to the values versus reversible hydrogen electrode.

The Koutecky-Levich equation was used for the electron transfer number (*n*) calculation, the detailed formula can be obtained in references [1,31]. To further verify the ORR mechanism, the peroxide percentage and the number were calculated based on the equations in references [1,31]. The kinetic current for Tafel plot was calculated according to the equation shown in reference [1].

### 2.4. Electrochemical test of Al-air batteries

For Al-air full batteries test, a polished aluminum stripe was used as anode, a 6 mol L<sup>-1</sup> KOH solution containing 0.01 mol L<sup>-1</sup>  $\text{Na}_2\text{SnO}_3$ , 0.0075 mol L<sup>-1</sup> ZnO and 0.0005 mol L<sup>-1</sup>  $\text{In}(\text{OH})_3$  was used as electrolyte. The air electrodes were composed of gas diffusion layer, foam nickel current collector and catalytic layer. The catalytic layer was fabricated as follows. The as-prepared catalysts (60 mg) and the 60 wt% polytetrafluoroethylene (PTFE) aqueous solution (50 mg) were mixed and agitated continuously until a paste appeared, and then rolled with glass rod until it turned into a film with the size of 2 × 2 cm. In the end, the film and gas diffusion layer were pressed onto the two sides of nickel foam under the pressure of 15 MPa, and dried at 60 °C for overnight. For comparison, the air electrode using commercial 20 wt% Pt/C catalyst was also fabricated with the same method. The full battery performance was measured with Neware battery testing system (Shenzhen, China). A home-made electrochemical cell was used for Al-air battery measurements, with the net volume size of 50 × 32 × 50 mm and a 10 mm diameter air hole was used for the test. Other details can be seen in our previous references [2,31,32].

## 3. Results and discussion

**Fig. 1(a)** shows the XRD patterns of Cu-N-KB-acid, Cu-KB and N-KB. **Fig. 1(b)** shows the XRD patterns of Cu-N-KB, Cu-N and the PDF cards. As shown in **Fig. 1(b)**, Cu-N-KB catalyst shows a broad diffraction peak at about 26°, which is assigned to carbon (0 0 2) [19,33]. There are two other phases existing in Cu-N-KB, Cu and  $\text{Cu}_2\text{S}$ . The sharp peaks at 43.3°, 50.45°, 74.1° are well indexed to metallic Cu (PDF#97-006-4699), demonstrating that a certain amount of  $\text{Cu}^{2+}$  was efficiently reduced to Cu during the synthesis process. The weak peaks at 32.64°, 37.4°, 39.05°, 45.9°, 48.4° can be indexed to the chalcocite  $\text{Cu}_2\text{S}$  (PDF#97-002-3596). For the pattern of Cu-N-KB-acid in **Fig. 1(a)**, no obvious peaks of Cu phase and  $\text{Cu}_2\text{S}$  phase are observed except the broad diffraction peak of

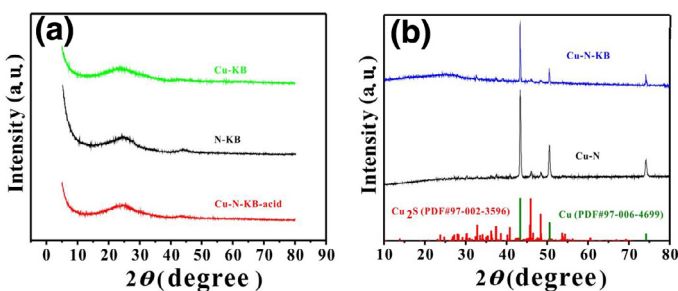


**Fig. 1.** (a) XRD patterns of Cu-N-KB-acid, Cu-KB and N-KB; (b) XRD patterns of Cu-N-KB, Cu-N and PDF cards. Raman spectroscopy technique was used to study structure change of the carbon materials.

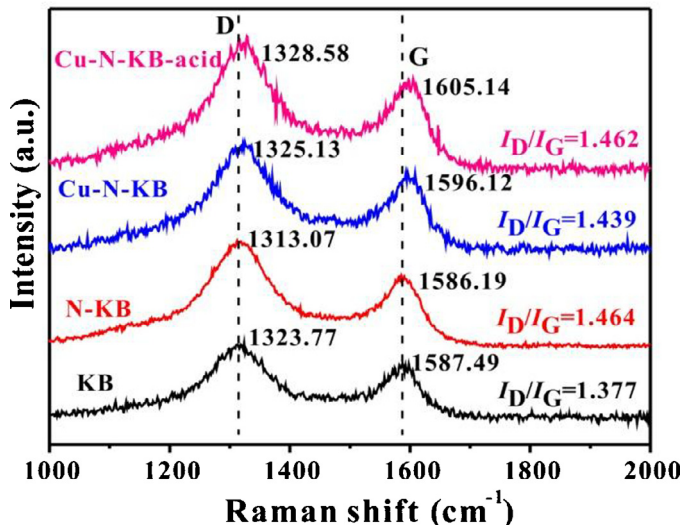


**Fig. 2.** Raman spectra of KB, N-KB, Cu-N-KB and Cu-N-KB-acid.

carbon (0 0 2) at about 26° [19,33]. This indicates that Cu and Cu<sub>2</sub>S are basically removed by acid treatment. For comparison, the XRD patterns of N-KB, Cu-KB and Cu-N are also analyzed. As seen, the N-KB and Cu-KB exhibit only typical carbon (0 0 2) peak at about 26° while Cu-N shows the typical Cu and chalcocite Cu<sub>2</sub>S phase. The results demonstrate that the formation of metallic Cu and chalcocite Cu<sub>2</sub>S are ascribed to the possible reaction between copper sulfate and melamine.

As observed in Fig. 2, the KB shows two obvious peaks at 1323.77 and 1587.49 cm<sup>-1</sup>, corresponding to the typical D-band and G-band peaks of carbon material [8,34]. For N-KB, the two peaks shift to the 1313.07 and 1586.19 cm<sup>-1</sup>, respectively. As reported, this red shift phenomenon is a general feature for N-doping carbon materials [31,35]. That is to say, nitrogen is successfully doped into the carbon via the incorporation of melamine as nitrogen source. The intensity ratio  $I_D/I_G$  of N-KB is 1.464, much higher than that of KB (1.377), indicating the greatly increased deficiency degree of the carbon frame. It is well known that nitrogen doping into the carbon causes structural defects and edge plane exposures in the carbon frame, which greatly facilitates the ORR [7,9,35,36]. For Cu-N-KB, the D-band and G-band peaks are blue-shifted to 1325.13 and 1596.12 cm<sup>-1</sup>, which should be ascribed to the higher vibration energy caused by copper doping. The  $I_D/I_G$  value of Cu-N-KB is 1.439, smaller than that of N-KB, indicating a higher crystallinity of the carbon frame. The similar phenomenon was also reported in Ref. [8]. It may be caused by the catalytic effect of Cu nanoparticles on the graphitization of carbon material during pyrolysis, just like Fe particles catalyzing the growth of carbon nanotubes and graphene as reported in references [37–39]. The  $I_D/I_G$  value of Cu-N-KB-acid is 1.462, higher than that of Cu-N-

KB, which should be due to the acid treatment that dissolves most Cu and Cu<sub>2</sub>S particles and probably increases the structural defects and edge plane exposures in the carbon frame [18,40].

Fig. S1 shows the TEM (a, b), HRTEM (c) images of Cu-N-KB. Fig. S2 shows the HADDF (a) and STEM-EDS elemental mapping images (b, c) of Cu-N-KB. Big particles (about 0.96–1.33 μm) are observed clearly in Fig. S1(a). As seen in the element mapping results in Fig. S2, the big particles should mainly be the metallic copper particles. The agglomeration of the Cu particles during the pyrolysis process causes the big sizes. After magnification, the KB-based nanoparticles with the size of 42–73 nm can be seen in Fig. S1(b). The lattice distances in Fig. S1(c) are determined to be 0.209 nm, corresponding to the Cu (1 1 1) plane. As seen in Fig. S2, the C and N elements are uniformly dispersed in Cu-N-KB, but Cu element is mainly focused on some big particles, being in accordance with the images in Fig. S1(a).

Fig. 3 shows the TEM (a), HRTEM (b), HADDF (c) and STEM-EDS elemental mapping images ((d)–(f)) of Cu-N-KB-acid. As seen in Fig. 3(a), the Cu-N-KB-acid is mainly composed of nanoparticles (KB particles) and a few darker particles with a diameter of about 60 nm are observed. According to the STEM-EDS elemental mapping images in Fig. 3(f), these darker particles should be copper containing substances. Fig. 3(b) shows the magnified HRTEM, which is within the area marked with red circle in the inset. The lattice plane of Cu (1 1 1) is verified to exist in Cu-N-KB-acid. By comparing the TEM images of Cu-N-KB-acid in Fig. 3(a) with those of Cu-N-KB (Fig. S1), it can be deduced that the acid treatment dissolves the big particles but leaves the smaller ones that encapsulated within the carbon layer (Fig. 3(a) and (b)). As discussed above, the big particles are mainly the metallic Cu particles, which can be further verified by the strong XRD signals of metallic Cu phase in Fig. 1. The small particles are mainly composed of two kinds of copper containing particles, one of which is the metallic copper particles. Previous references have disclosed that metallic Fe/Co and their nitrides embedded into carbon layers are important active sites for ORR [1,2,18,31,41,42]. The metallic Cu particles encapsulated within carbon layer are herein believed as important active sites for ORR [43,44]. The other type of the small particles is the noncrystalline Cu<sub>N</sub><sub>x</sub>C<sub>y</sub> species. As confirmed by the elemental mapping images (Fig. 3(d)–(f)), the C, N and Cu elements are uniformly dispersed in selected area, suggesting the successful doping of Cu and N into the carbon supports and facilitating the formation of the noncrystalline Cu<sub>N</sub><sub>x</sub>C<sub>y</sub> moieties in the composite [41]. The existence of noncrystalline Cu<sub>N</sub><sub>x</sub>C<sub>y</sub> moieties is further verified in the XPS spectrum in Fig. 4.

XPS was used to investigate the elemental compositions and valence states. As seen in Fig. 4(a), Cu-N-KB exhibits three apparent peaks of C 1s, Cu 2p, and N 1s, as well as a weak peak of S 2p. For Cu-N-KB-acid, the Cu 2p peak decreases greatly and the S 2p almost disappears due to the removal of unstable Cu and Cu<sub>2</sub>S nanoparticles during the acid treatment. The signal of N 1s in Cu-N-KB-acid (Fig. 4(c)) is fitted into four peaks at 398.5 eV, 400.4 eV, 401.4 eV and 399.1 eV, corresponding to pyridinic nitrogen, pyrrolic nitrogen, graphitic nitrogen and metal-coordinated nitrogen [29,45–47], respectively. The total content of nitrogen is about 1.56 at% (Table S1). The contents of the four types of nitrogen are 25.57 at%, 27.69 at%, 33.95 at% and 12.79 at%, respectively, according to the Gaussian fitting results (Table S2). As reported, the doped nitrogen plays important roles on ORR [11,29,45,48–50]. Moreover, the copper-bonded nitrogen greatly contribute to the ORR catalytic activity [8,19,25,33,51], the same as the iron-bonded nitrogen [3,8,20,34,52–54]. Note that the copper-bonded nitrogen is another kind of pyridinic nitrogen, whose lone pair electrons coordinate with Cu to form the Cu<sub>N</sub><sub>x</sub>C<sub>y</sub> active moieties [41]. The C 1s spectrum of Cu-N-KB-acid (Fig. 4(b)) is fitted into two peaks at 284.85 eV and 286.2 eV, relating to the *sp*<sup>2</sup> graphitic

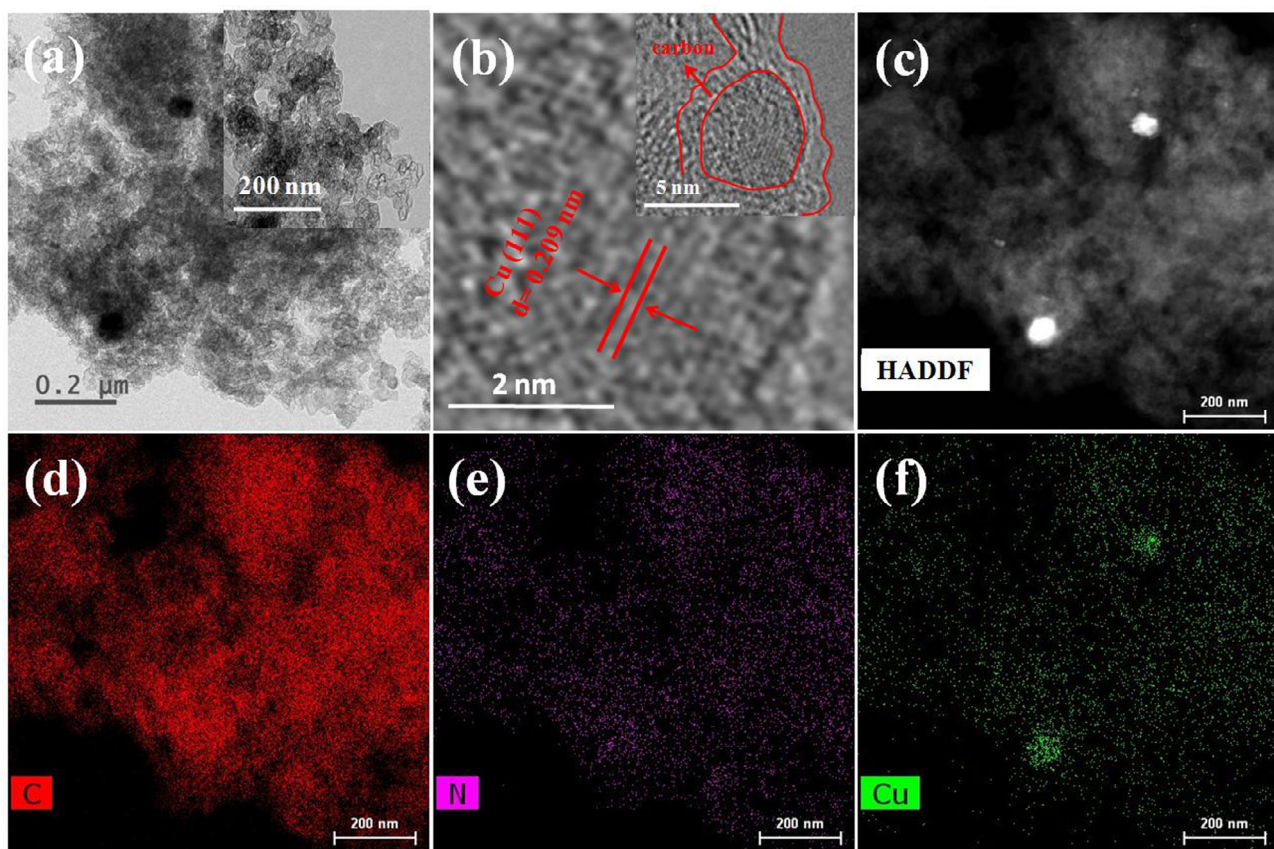


**Fig. 3.** The TEM (a), HRTEM (b), HADDF (c) and the STEM-EDS elemental mapping images (d-f) of Cu-N-KB-acid.

carbon [55] and C–O bond [1,56], respectively. For O 1s spectrum of Cu-N-KB-acid, no metal–oxygen bond (~530.2 eV) [2,57] but low-oxygen defect sites (531.63 eV) [2,58] and physically adsorbed water (532.9 eV) [2,59] are observed in Fig. S3(a). No obvious signal of S 2p in Cu-N-KB-acid is observed (Fig. 4(d)) when compared with that in Cu-N-KB (Fig. S3b), due to the dissolution of cuprous sulfide during the acid treatment. The binding energy spectra of Cu 2p for Cu-N-KB-acid and Cu-N-KB are shown in Fig. 4(e) and (f), respectively. As seen, the signal of Cu-N-KB-acid is much weaker than that of Cu-N-KB, which is well fitted to six peaks at 933.6 eV ( $\text{Cu}^0$ ,  $2p_{3/2}$ ), 934.6 eV ( $\text{Cu}^{2+}-\text{N}_x$ ,  $2p_{3/2}$ ), 942.9 eV (satellite peak), 953.45 eV ( $\text{Cu}^0$ ,  $2p_{1/2}$ ), 956.4 eV ( $\text{Cu}^{2+}-\text{N}_x$ ,  $2p_{1/2}$ ) and 963.4 eV (satellite peak), respectively [3,19,33,34,60]. It is noted that the valence state of copper element in Cu-N-KB-acid catalyst should be the same with that of Cu-N-KB, mainly  $\text{Cu}^0$  and  $\text{Cu}^{2+}-\text{N}_x$ . According to the TEM-EDS results (Table S1), the copper contents in Cu-N-KB-acid and Cu-N-KB are 0.37 at% and 12.34 at%, respectively, indicating that most unstable Cu-based species were removed by the acid treatment.

The  $\text{N}_2$  adsorption–desorption isotherm and the corresponding pore size distribution plot of Cu-N-KB-acid are shown in Fig. 5. As seen in Fig. 5(a), Cu-N-KB-acid shows a typical hysteresis loop of type H<sub>4</sub> (IUPAC), indicating the existence of mesopores [11,17,29,61]. The specific surface area is calculated to be 653.9 m<sup>2</sup> g<sup>-1</sup>, using the Brunauer–Emmett–Teller (BET) equation from the data of adsorption isotherm. The pore diameter distribution is analyzed by nonlocal density functional theory (NLDFT) and ranges from 0.61 to 35.9 nm, mainly focusing at 4.27 nm, as shown in Fig. 5(b).

The LSV curves for different samples at a rotating speed of 1600 rpm are shown in Fig. 6(a). It is clearly seen that Cu-N-KB exhibits superior catalytic activity to Cu-KB, Cu-N, N-KB and

KB, with more positive onset potential (0.92 V vs. RHE) and half-wave potential (0.80 V vs. RHE), larger limiting current density (~6.0 mA cm<sup>-2</sup>). As observed, KB alone possesses very poor ORR catalytic activity. After the incorporation of Cu or N species, both Cu-KB and N-KB exhibit improved the ORR activity. For Cu-N, it exhibits the lowest ORR catalytic activity. After the incorporation of KB into Cu-N, the ORR activity of Cu-N-KB is significantly enhanced. The Cu-N-KB-acid shows almost the same onset potential and half-wave potential with Cu-N-KB, but a little higher and more stable limiting current density. In spite of the removal of most Cu/Cu<sub>2</sub>S species (the active sites for ORR [33,62,63]), Cu-N-KB-acid still shows a little better catalytic performance than Cu-N-KB. This phenomenon can be explained as follows. First, it is the big-sized copper particles, which generally possess much poorer catalytic activity due to the size effect [35,36,64], dissolved by the acid treatment. While those nanoparticles with higher efficient ORR activity were wrapped by carbon layer and could not be removed. The decay of catalytic activity because of the dissolution of the unstable Cu/Cu<sub>2</sub>S is negligible. Second, acid treatment to the catalyst probably leads to the increase of structural defect and edge plane exposure in the carbon frame [18,40]. This is also verified in the Raman spectrum in Fig. 2. As can be seen, the  $I_D/I_G$  value of Cu-N-KB-acid is higher than that of Cu-N-KB, suggesting the increased structural defects and edge plane exposure in the carbon frame after acid treatment. It is believed that a good balance is achieved for the acid treated sample here. As observed, the ORR performance of Cu-N-KB-acid is comparable to that of 20% Pt/C (~0.82 V of half-wave potential and ~5.5 mA cm<sup>-2</sup> of limiting current density). It is also comparable to those recently reported Cu-N-C catalysts [8,19,33]. Based on the comparison results of different control samples, it is clear that the incorporation of Cu source and N sources into the KB, largely contributes to the significantly improved ORR perfor-

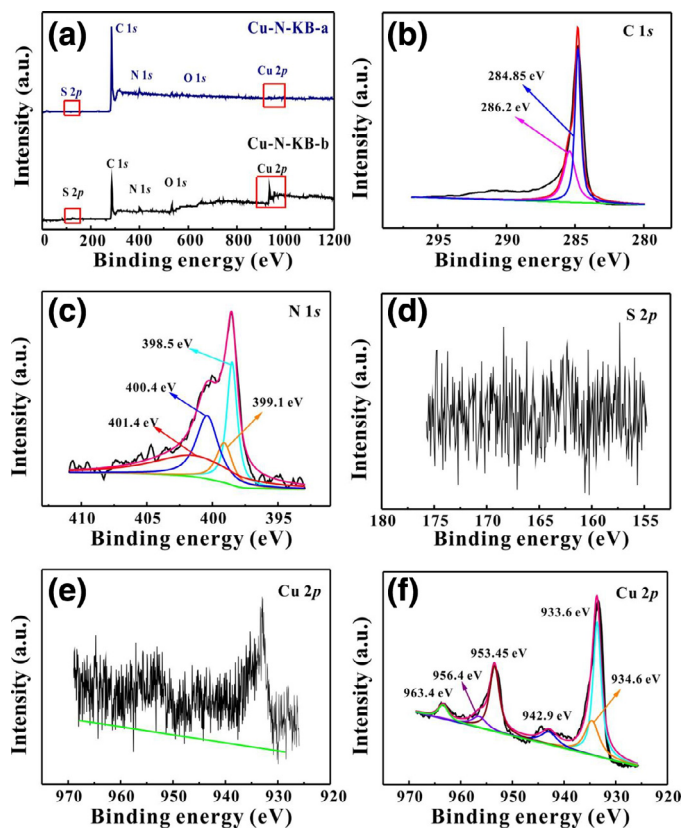


**Fig. 4.** (a) The survey XPS spectra for Cu-N-KB-acid and Cu-N-KB; XPS spectra of the (b) C 1s, (c) N 1s, (d) S 2p, (e) Cu 2p for Cu-N-KB-acid, and (f) Cu 2p for Cu-N-KB.

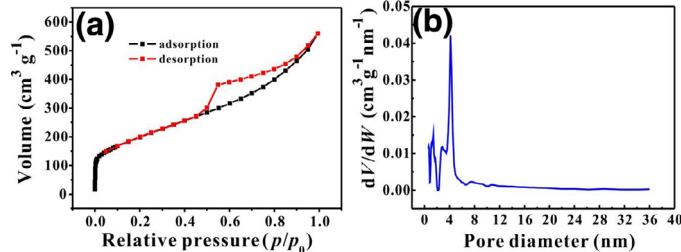


**Fig. 5.** (a)  $N_2$  adsorption–desorption isotherm and (b) the pore size distribution plot of Cu-N-KB-acid.

mance. As a matter of fact, both the non-crystalline  $FeN_xC_y$  moieties and the crystalline metal-based nanoparticles (e.g.  $Fe/Fe_3C$ ) encased in surrounding graphitic carbon layers have been proposed as the main active sites for Fe-N-C catalysts [41,45,65–67]. We believe that the Cu-N-C catalyst reported in this work obeys similar catalytic mechanism with the Fe-N-C in references [8,19].

Fig. 6(b) shows the LSV curves of Cu-N-KB-acid at different rotating speeds, and the inset is K-L plots based on these curves. It can be seen that the K-L plots are almost parallel with each other, indicating similar electron transfer numbers for ORR in the electrolyte at different potentials [2,68–71]. The electron transferred number of Cu-N-KB-acid calculated from K-L equation is averagely 3.92, confirming a four-electron pathway. As shown in Fig. 6(c), the Tafel slope of Cu-N-KB-acid is 71.3 mV per decade, suggesting similar kinetic behavior with Pt/C (82.2 mV per decade). To further verify the ORR mechanism obtained from Fig. 6(b), the rotating-ring-disk electrode (RRDE) tests were performed. As seen in Fig. 6(d), the  $n$  values of Cu-N-KB-acid shown in Fig. 6(f) are ~3.84 to 3.94 from 0.2 to 0.8 V (vs. RHE), confirming a 4e oxygen reduction

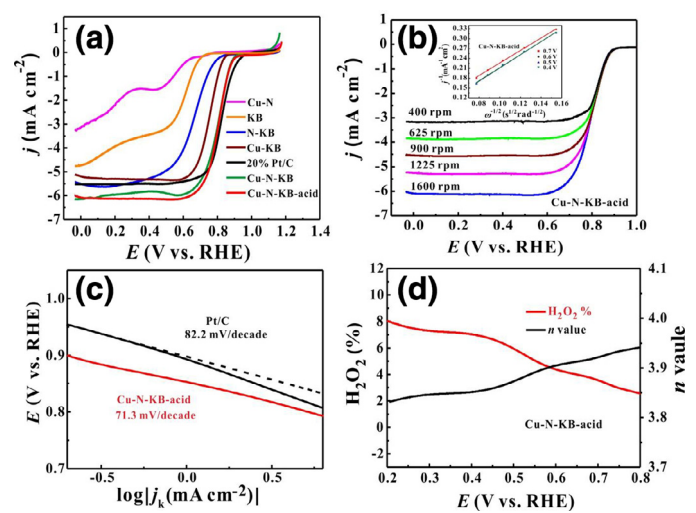


**Fig. 6.** (a) LSV curves of Cu-N, KB, N-KB, Cu-KB, Cu-N-KB, Cu-N-KB-acid and 20% Pt/C on RDE in  $O_2$ -saturated 0.1 M KOH solution at a scan rate of  $10\text{ mV s}^{-1}$  with a rotation speed of 1600 rpm; (b) LSV curves at different rotating speeds in  $O_2$ -saturated 0.1 M KOH solution at a scan rate of  $10\text{ mV s}^{-1}$  and K-L plots (inset) for Cu-N-KB-acid; (c) Tafel plots of kinetic current for Cu-N-KB-acid and 20% Pt/C; (d) percentage of peroxide ( $H_2O_2\%$ ) and electron transfer number ( $n$ ) of Cu-N-KB-acid.

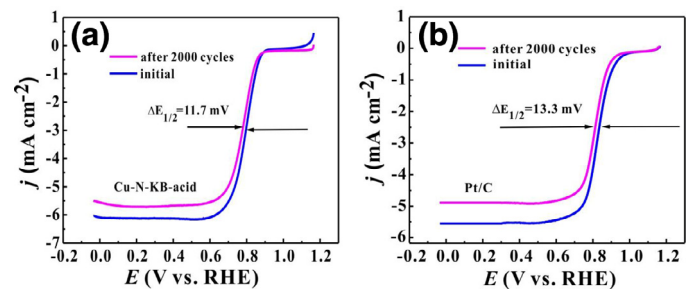


**Fig. 7.** LSV curves of (a) Cu-N-KB-acid and (b) 20% Pt/C before and after the accelerated durability test (ADT). The ADT was performed by subjecting catalyst to 2000 cycles from 0.565 to 1.165 V (vs. RHE) in  $O_2$ -saturated 0.1 M KOH solution at room temperature at a scan rate of  $100\text{ mV s}^{-1}$ .

mechanism. To further make certain the electrode-reaction process of the Cu-N-KB-acid, CV test was performed in  $O_2$ -saturated and Ar-saturated 0.1 M KOH solution, respectively. As seen in Fig. S4, a strong ORR peak (~0.80 V) is observed for Cu-N-KB-acid in  $O_2$ -saturated 0.1 M KOH solution and no peak appears in Ar-saturated 0.1 M KOH solution. It demonstrates that Cu-N-KB-acid is very stable in the testing condition.

The stability of Cu-N-KB-acid for ORR was evaluated by the half-wave potential decay ( $\Delta E_{1/2}$ ) before and after the accelerated durability test (ADT). The ADT was performed by subjecting catalyst to 2000 cycles from 0.565 to 1.165 V (vs. RHE) in  $O_2$ -saturated 0.1 M KOH solution at room temperature with a scan rate of  $100\text{ mV s}^{-1}$ . As shown in Fig. 7(a), the half-wave potential of Cu-N-KB-acid exhibits a negative shift of ~11.7 mV after 2000 cycles, slightly less than that of 20% Pt/C (Fig. 7(b), ~13.3 mV) and much less than that of Cu-N-KB (~32 mV) (Fig. S5). The results reveal that the acid treatment not only strengthens the ORR activity, but also improves the durability of the catalyst.

To further evaluate the practical catalytic performance of Cu-N-KB-acid in Al-air battery, the cell voltage at various current densities and the constant current discharge tests were carried out. The commercial Pt/C and Cu-N-KB were also investigated for comparison. As observed in Fig. 8(a), the cell voltages with these three kinds of catalysts all decrease with the increase of current density. When the current density is lower than  $80\text{ mA cm}^{-2}$ , the cell

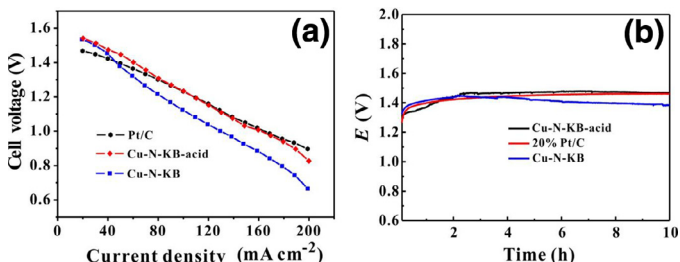


**Fig. 8.** Cell voltages of Al-air batteries with different cathode catalysts at various current densities (a) and discharge curves at a constant current density of  $50 \text{ mA cm}^{-2}$  (b).

voltage with Cu-N-KB-acid is slightly higher than that with Pt/C. At the range of  $80\text{--}140 \text{ mA cm}^{-2}$ , the cell voltage with Cu-N-KB-acid is almost equal to that with Pt/C. It is clear that the cell voltage with Cu-N-KB is lower than those with Cu-N-KB-acid and Pt/C when current density is higher than  $50 \text{ mA cm}^{-2}$ . As seen in Fig. 8(b), Cu-N-KB-acid catalyst exhibits an increasing tendency of discharge voltage in the initial 2.5 h until to a stable voltage of about 1.47 V, due to the activation process of Al anode, on which the passive film was dissolved gradually [2]. The Pt/C behaves the same as Cu-N-KB-acid in the first 2.5 h until to the voltage of  $\sim 1.45 \text{ V}$ , which is about 20 mV lower than that of Cu-N-KB-acid. As for the Cu-N-KB, it shows a decreasing discharge voltage after arriving to the highest voltage ( $\sim 1.44 \text{ V}$ ). In home-made Al-air batteries, the as-prepared Cu-N-KB-acid even exhibited a little higher discharge voltage than the commercial Pt/C.

#### 4. Conclusions

In summary, KB-supported Cu nanoparticles and noncrystalline  $\text{CuN}_x\text{C}_y$  composite catalyst was synthesized by a facile hydrothermal method with cheap and eco-friendly raw materials and subsequent pyrolysis process. When used as a catalyst for ORR, this as-prepared composite favored four-electron pathway in  $0.1 \text{ M KOH}$  solution, exhibiting a comparable catalytic activity and superior stability to the commercial Pt/C. It is believed that the good related effects of Cu nanoparticles, noncrystalline  $\text{CuN}_x\text{C}_y$  species and KB supports greatly contribute to such super ORR activity. When used in Al-air full cell, it even exhibited a little higher discharge voltage ( $\sim 1.47 \text{ V}$ ) than the commercial Pt/C ( $\sim 1.45 \text{ V}$ ) at a discharge current density of  $50 \text{ mA cm}^{-2}$ . The strategy here using Cu-N-C species to boost the ORR performance of carbon supports can provide a good clue for developing low-cost but highly efficient catalyst materials in Al-air batteries.

#### Acknowledgments

This work was supported by the National Natural Science Foundation of China (nos. 21671200 and 21571189), Fujian Provincial Natural Science Foundation of China (no. 2015J01072), the Hunan Provincial Science and Technology Plan Project, China (no. 2016TP1007) and Innovation-Driven Project of Central South University (no. 2016CXS009).

#### Supplementary materials

Supplementary material associated with this article can be found, in the online version, at doi:10.1016/j.jechem.2017.12.002.

#### References

- [1] J. Li, Z. Zhou, K. Liu, F. Li, Z. Peng, Y. Tang, H. Wang, J. Power Sources 343 (2017) 30–38.
- [2] K. Liu, X. Huang, H. Wang, F. Li, Y. Tang, J. Li, M. Shao, ACS Appl. Mater. Interfaces 8 (2016) 34422–34430.
- [3] F. Wang, Y. Zhao, P. Wei, Q. Zhang, J. Liu, A. Alfantazi, Chem. Commun. 53 (2017) 1514–1517.
- [4] Q. Li, N.J. Bjerrum, J. Power Sources 110 (2002) 1–10.
- [5] W.A. Ferrando, J. Power Sources 130 (2004) 309–314.
- [6] J. Ma, J. Wen, J. Gao, Q. Li, Electrochim. Acta 129 (2014) 69–75.
- [7] S. Zhong, C. Zhan, D. Cao, Carbon 85 (2015) 51–59.
- [8] H. Yu, A. Fisher, D. Cheng, D. Cao, ACS Appl. Mater. Interfaces 8 (2016) 21431–21439.
- [9] D. Guo, R. Shibuya, C. Akiba, S. Saji, T. Kondo, J. Nakamura, Science 351 (2016) 361–365.
- [10] G. Zhang, W. Lu, F. Cao, Z. Xiao, X. Zheng, J. Power Sources 302 (2016) 114–125.
- [11] Y. Wu, S. Zhao, K. Zhao, T. Tu, J. Zheng, J. Chen, H. Zhou, D. Chen, S. Li, J. Power Sources 311 (2016) 137–143.
- [12] Y. Liu, H. Jiang, Y. Zhu, X. Yang, C. Li, J. Mater. Chem. A 4 (2016) 1694–1701.
- [13] Q. Yi, Y. Zhang, X. Liu, B. Xiang, Y. Yang, J. Mater. Sci. 49 (2013) 729–736.
- [14] H. Wang, Z. Zhang, Y. Yang, K. Wang, S. Ji, J. Key, Y. Ma, R. Wang, J. Solid State Electrochem. 19 (2015) 1727–1733.
- [15] J. Sanetuntikul, S. Shanmugam, Nanoscale 7 (2015) 7644–7650.
- [16] Y. Xie, H. Li, C. Tang, S. Li, J. Li, Y. Lv, X. Wei, Y. Song, J. Mater. Chem. A 2 (2014) 1631–1635.
- [17] W. Yang, X. Yue, X. Liu, L. Chen, J. Jia, S. Guo, Nanoscale 8 (2016) 959–964.
- [18] J. Li, J. Chen, H. Wang, Y. Ren, K. Liu, Y. Tang, M. Shao, Energy Storage Mater. 8 (2017) 49–58.
- [19] H. Wu, H. Li, X. Zhao, Q. Liu, J. Wang, J. Xiao, S. Xie, R. Si, F. Yang, S. Miao, X. Guo, G. Wang, X. Bao, Energy Environ. Sci. 9 (2016) 3736–3745.
- [20] K. Cho, S.H. Han, M.P. Suh, Angew. Chem. Int. Ed. 55 (2016) 15301–15305.
- [21] A.P. Periasamy, W. Wu, G. Lin, Z. Shih, Z. Yang, H. Chang, J. Mater. Chem. A 2 (2014) 11899–11904.
- [22] W.H. Lee, D.W. Lee, H. Kim, J. Electrochem. Soc. 162 (2015) F744–F749.
- [23] C.H. Wang, H.C. Huang, S.T. Chang, Y.C. Lin, M.F. Huang, RSC Adv. 4 (2013) 4207–4211.
- [24] R. Chen, W. Zhao, L. Qian, M. Pan, Acta Phys. Chim. Sin. 29 (2013) 792–798.
- [25] H. Wu, W. Chen, J. Am. Chem. Soc. 133 (2011) 15236–15239.
- [26] W. Yang, X. Liu, X. Yue, J. Jia, S. Guo, J. Am. Chem. Soc. 137 (2015) 1436–1439.
- [27] W. Ding, L. Li, K. Xiong, Y. Wang, W. Li, Y. Nie, S. Chen, X. Qi, Z. Wei, J. Am. Chem. Soc. 137 (2015) 5414–5420.
- [28] Y. Hu, J.O. Jensen, W. Zhang, L.N. Cleemann, W. Xing, N.J. Bjerrum, Q. Li, Angew. Chem. Int. Ed. 53 (2014) 3675–3679.
- [29] J. Zhang, D. He, H. Su, X. Chen, M. Pan, S. Mu, J. Mater. Chem. A 2 (2014) 1242–1246.
- [30] Y. Su, H. Jiang, Y. Zhu, X. Yang, J. Shen, W. Zou, J. Chen, C. Li, J. Mater. Chem. A 2 (2014) 7281–7287.
- [31] K. Liu, Z. Zhou, H. Wang, X. Huang, J. Xu, Y. Tang, J. Li, H. Chu, J. Chen, RSC Adv. 6 (2016) 55552–55559.
- [32] H. Zhang, H. Qiao, H.Y. Wang, N. Zhou, J.J. Chen, Y.G. Tang, J.S. Li, C.H. Huang, Nanoscale 6 (2014) 10235–10242.
- [33] S.H. Noh, M.H. Seo, X. Ye, Y. Makinose, T. Okajima, N. Matsushita, B. Han, T. Ohsaka, J. Mater. Chem. A 3 (2015) 22031–22034.
- [34] F.F. Wang, P.J. Wei, G.Q. Yu, J.G. Liu, Chemistry 22 (2016) 382–389.
- [35] A. Zahoor, M. Christy, J.H. Yun, R.L. Yi, P. Kim, K.S. Nahm, Appl. Catal. B 147 (2014) 633–641.
- [36] L.S. Panchakarla, A. Govindarajan, C.N. Rao, ACS Nano. 1 (2007) 494–500.
- [37] Y. Qiu, J. Yu, W. Wu, J. Yin, X. Bai, J. Solid State Electrochem. 17 (2012) 565–573.
- [38] H. An, W.J. Lee, J. Jung, Curr. Appl. Phys. 11 (2011) S81–S85.
- [39] G. Ning, Y. Liu, F. Wei, Q. Wen, G. Luo, J. Phys. Chem. C 111 (2007) 1969–1975.
- [40] A. Shen, Y. Zou, Q. Wang, R.A. Dryfe, X. Huang, S. Dou, L. Dai, S. Wang, Angew. Chem. Int. Ed. 53 (2014) 1–6.
- [41] K. Liu, Z. Peng, H. Wang, Y. Ren, D. Liu, J. Li, Y. Tang, N. Zhang, J. Electrochem. Soc. 164 (2017) F475–F483.
- [42] H. Zhang, H. Li, H. Wang, K. He, S. Wang, Y. Tang, J. Chen, J. Power Sources 280 (2015) 640–648.
- [43] H.H. Li, C.H. Cui, S. Zhao, H.B. Yao, M.R. Gao, F.J. Fan, S.H. Yu, Adv. Energy Mater. 2 (2012) 1182–1187.
- [44] K. Jiang, P. Wang, S. Guo, X. Zhang, X. Shen, G. Lu, D. Su, X. Huang, Angew. Chem. Int. Ed. 55 (2016) 9030–9035.
- [45] S. Yasuda, A. Furuya, Y. Uchibori, J. Kim, K. Murakoshi, Adv. Funct. Mater. 26 (2016) 738–744.
- [46] E.J. Biddinger, D.V. Deak, U.S. Ozkan, Top. Catal. 52 (2009) 1566–1574.
- [47] S. Pylypenko, S. Mukherjee, T.S. Olson, P. Atanassov, Electrochim. Acta 53 (2008) 7875–7883.
- [48] H. Peng, Z. Mo, S. Liao, H. Liang, L. Yang, L. Fan, H. Song, Y. Zhong, B. Zhang, Sci. Rep. 3 (2013) 1765–1771.
- [49] H.S. Oh, H. Kim, J. Power Sources 212 (2012) 220–225.
- [50] H. Kim, K. Lee, S.I. Woo, Y. Jung, Phys. Chem. Chem. Phys. 13 (2011) 17505–17510.
- [51] S.H. Noh, D.H. Kwak, H.S. Min, T. Ohsaka, B. Han, Electrochim. Acta 140 (2014) 225–231.
- [52] Y. Zhang, L. Huang, W. Jiang, X. Zhang, Y. Chen, Z. We, L. Wanac, J. Hu, J. Mater. Chem. A 4 (2016) 7781–7787.
- [53] X. Zhao, F. Li, R. Wang, J. Seo, H. Choi, S. Jung, J. Mahmood, I.Y. Jeon, J.B. Baek, Adv. Funct. Mater. 27 (2017) 160571–160577.
- [54] C. Du, X. Gao, W. Chen, Chin. J. Catal. 37 (2016) 1049–1061.

- [55] Z. Zhang, L. Su, M. Yang, M. Hu, J. Bao, J. Wei, Z. Zhou, *Chem. Commun.* 50 (2014) 776–778.
- [56] N. Daems, X. Sheng, I.F.J. Vankelecom, P.P. Pescarmona, *J. Mater. Chem. A* 2 (2013) 4085–4110.
- [57] J.F. Marco, J.R. Gancedo, M. Gracia, J.L. Gautier, E. Rios, F.J. Berry, *J. Solid State Chem.* 153 (2000) 74–81.
- [58] X.F. Lu, D.J. Wu, R.Z. Li, Q. Li, S.H. Ye, Y.X. Tong, G.R. Li, *J. Mater. Chem. A* 2 (2014) 4706–4713.
- [59] T. Choudhury, S.O. Saeid, J.L. Sullivan, A.M. Abbot, *J. Phys. D Appl. Phys.* 22 (2000) 1185–1195.
- [60] L. Han, P. Wang, H. Liu, Q. Tan, J. Yang, *J. Mater. Chem. A* 4 (2016) 18354–18365.
- [61] Y. Li, H. Zhang, Y. Wang, P. Liu, H. Yang, X. Yao, D. Wang, Z. Tang, H. Zhao, *Energy Environ. Sci.* 7 (2014) 3720–3726.
- [62] X. Wang, Y. Ke, H. Pan, K. Ma, Q. Xiao, D. Yin, G. Wu, M.T. Swihart, *ACS Catal.* 5 (2015) 2534–2540.
- [63] M. Seredych, E. Rodriguez-Castellon, T.J. Bandosz, *J. Mater. Chem. A* 2 (2014) 20164–20176.
- [64] L. Zhang, K. Lee, J. Zhang, *Electrochim. Acta* 52 (2007) 7964–7971.
- [65] D. Singh, K. Mamiani, C.R. Bruening, J.T. Miller, U.S. Ozkan, *ACS Catal.* 4 (2014) 3454–3462.
- [66] J. Masa, W. Xia, M. Muhler, W. Schuhmann, *Angew. Chem. Int. Ed.* 54 (2015) 10102–10120.
- [67] A. Zitolo, V. Goellner, V. Armel, M.-T. Sougrati, T. Mineva, L. Stievano, E. Fonda, F. Jaouen, *Nat. Mater.* 14 (2015) 937–944.
- [68] K.J.J. Mayrhofer, D. Strmcnik, B.B. Blizanac, V. Stamenkovic, M. Arenz, N.M. Markovic, *Electrochim. Acta* 53 (2008) 3181–3188.
- [69] S.S. Li, H.P. Cong, P. Wang, S.H. Yu, *Nanoscale* 6 (2014) 7534–7541.
- [70] K. Lei, X. Han, Y. Hu, X. Liu, L. Cong, F. Cheng, J. Chen, *Chem. Commun.* 51 (2015) 11599–11602.
- [71] J. Xiao, Q. Kuang, S. Yang, F. Xiao, S. Wang, L. Guo, *Sci. Rep.* 3 (2013) 2300.